Supporting Information

Cooperating Oxidation of NH_3 and H_2O to Selectively Produce Nitrate via a Nearly Barrierless N–O Coupling Pathway

Kun Dang,[1,2] Lei Wu,[1,2] Siqin Liu,[1,2] Hongwei Ji,[1,2] Chuncheng Chen,[1,2] Yuchao Zhang,[1,2]* and Jincai Zhao[1,2]

[1] Key Laboratory of Photochemistry, CAS Research/Education Center for Excellence in Molecular Sciences, Institute of Chemistry, Chinese Academy of Sciences, Beijing 100190 (P. R. China)

[2] University of Chinese Academy of Sciences, Beijing 100049 (P. R. China)

E-mail: yczhang@iccas.ac.cn

1. Experimental section

1.1. Reagents and materials

The n-Si (100) (1–10 Ω·cm, 300 μm) and p^+-Si (100) (0.001–0.005 Ω·cm, 500 μm) were purchased from the Zhejiang Lijing Optoelectronic Technology Co., Ltd. and Hefei KeJing Materials Technology Co., Ltd., respectively. $NiCl_2 \cdot 6H_2O$ (99.95%) and $NaClO_4$ (98%) were purchased from Alfa Aesar Chemical Co., Ltd. $CuSO_4 \cdot 5H_2O$ (> 99%) was purchased from Sinopharm Chemical Reagent Co., Ltd. The H_3BO_3 (99.5%), $NH_3 \cdot H_2O$, and Deuterium oxide (D_2O, 99.9 atom% D) were purchased from Beijing Innochem Technology Co., Ltd., and the NaOH (99.9%) was purchased from the Shanghai Aladdin Biochemical Technology Co., Ltd. ND_3 (25 wt.% in D_2O, 99% atom D) was purchased from Sigma-Aldrich, Co., Ltd. Sodium deuteroxide (NaOD, 40% solution in D_2O, > 99 atom% D), Sodium nitrate ($NaNO_3$, 99%), Sodium nitrite ($NaNO_2$, > 97%) were purchased from ACROS Organics. All chemicals were used as received without further purification. The ultrapure water with a resistivity of 18.2 MΩ·cm was obtained by purification equipment (Millipore, Milli-RO Plus).

1.2. Materials preparation

Synthesis of Ni/n-Si photoanode. The Si wafers were diced into 1 × 2 cm^2 rectangles and sonicated for 30 min in acetone, ethanol, and ultrapure water in sequence. Then the ohmic contact was prepared as follows: (1) The Si surface was freshly hydrogenated by dipping it for 2 min in an HF solution (H_2O/50% HF, V_1/V_2 = 5/1) and quickly dried under an N_2 flow; (2) Scratching one of Si surfaces and a droplet of In-Ga eutectic was applied on the scratched position to enhance contact, then it was covered by a layer of silver paste with a copper wire

inside. After drying the silver paste (~3 h), the Si surface with ohmic contact was covered by hot melt adhesive. For the electrodeposition of Ni nanoparticles, 0.1 M boric acid, and 0.01 M $NiCl_2 \cdot 6H_2O$ were dissolved in water in a 50 mL cell without oxygen removal, then sonicated the electrolyte for 20 min. In a three-electrode system, the cleaned Si was immersed in the electrolyte, with Pt foil (counter electrode) and Ag/AgCl (reference electrode). Applying −1.5 $V_{Ag/AgCl}$ on the Si electrode for 5 s to deposit the Ni nanoparticle protection layer, then the Si electrode was washed with water and dried with N_2 flow.

Synthesis of NiO/Ni/n-Si photoanode. The synthesis of NiO/Ni/n-Si photoanode was based on the as-prepared Ni/n-Si photoanode above. For the electrochemical deposition of NiO electrocatalyst, 4 mM $NiCl_2 \cdot 6H_2O$ served as the electrolyte without oxygen removal, and a constant potential of −0.8 $V_{Ag/AgCl}$ was applied to the Ni/n-Si till the 20 mC/cm^2 charge was passed through. Then the photoanode was washed with water and dried with air.

Synthesis of $NiCuO_x$/Ni/n-Si photoanode. The process for $NiCuO_x$/Ni/n-Si photoanode synthesis was the same as that for NiO/Ni/n-Si photoanode, but the electrolyte was changed to 0.4 mM $CuSO_4 \cdot 5H_2O$ in 4 mM $NiCl_2 \cdot 6H_2O$.

Synthesis of CuO_x/Ni/n-Si photoanode. The process for CuO_x/Ni/n-Si photoanode synthesis was the same as that for $NiCuO_x$/Ni/n-Si photoanode, but the electrolyte was replaced by 0.4 mM $CuSO_4 \cdot 5H_2O$ without any Ni^{2+} precursor.

1.3. Materials characterization

The morphology of photoanodes was characterized by the Scanning Electron Microscope (SEM, S4800, Hitachi) with 10 kV accelerating voltage. The valence states of Ni and O were obtained by the X-ray photoelectron spectroscopy (XPS, ESCALab 250Xi, Thermo Scientific) using 200 W monochromatic Al Kα radiation, where the hydrocarbon C1s line at 284.8 eV from adventitious carbon was used for calibration. For the HRTEM tests, the sample was first covered with a Tungsten protection layer, and it was then sliced by the FIB (Helios G4 FIB-SEM, Thermo Fisher). The HRTEM tests were carried out on the transmission electron microscope (FEI Talos F200X G2, Thermo Scientific) at 200 kV with a high-angle annular dark field detector.

1.4. Photoelectrochemical measurements

Most PEC measures were performed on the PGSTAT302N (Autolab, Metrohm) electrochemical workstation in a three-electrode sealed single-chamber cell with a circulator bath of 25 °C, under the illumination of a Xenon lamp (100 mW cm^{-2}) equipped with an AM 1.5 G filter. The Ag/AgCl electrode (filled with saturated KCl solution) was used as the reference electrode, and the Pt wire was the counter electrode. Potentials were converted to the reversible hydrogen electrode (RHE) scale according to the Nernst equation: $E_{RHE} = E_{Ag/AgCl} + 0.059 \times pH + 0.197$. The oxygen was removed from the electrolyte by bubbling Ar into the PEC cell for 15 min. The CV measurements were carried out at a scan rate of 50 mV/s, and the steady-state current was obtained using the chronoamperometry method with a duration of 60 s. For the electrolysis process, a constant potential was applied to the working electrode till the

total charge of 8 C was passed through. The products were analyzed using the method shown in "1.11. Products analysis".

1.5. Photoelectrochemical characterization

EIS measurements. For EIS measurements, a sinusoidal voltage pulse of 10 mV amplitude was applied on a bias potential, with frequencies ranging from 10 kHz to 0.1 Hz, under the illumination of a white LED (100 mW cm^{-2}). The raw data were fitted and simulated using Nova 2.1.4 software (Metrohm), and related data is exhibited in Table S1. The density of surface-trapped holes in Figure 1c of the manuscript was calculated via the following equation[1]:

$$[h^+] = C_{trap} \times V_{appl} \times \frac{R_{ct}}{R_s + R_{trapping} + R_{ct}} / (S \times q). \quad (1)$$

The $[h^+]$ (nm^{-2}) is the density of surface-trapped holes, V_{appl} (V_{RHE}) is the applied potential, S (nm^2) is the electrochemical active surface area (ECSA) of the photoanode, and q is the electron charge (1.6×10^{-19} C). The ECSA was estimated by dividing the electric double-layer capacitor by a standardized capacitance (3.7 μF cm^{-2}).[2]

Mott-Schottky measurement. The Mott-Schottky measurement was carried out in 1 M KCl + 50 mM $K_3Fe(CN)_6$ + 350 mM $K_4Fe(CN)_6$ at 0.5, 0.75 and 1.00 kHz in dark based on the Mott-Schottky equation:

$$\frac{1}{C^2} = \frac{2}{A^2 \varepsilon_0 \varepsilon_r q N_d} \left(E - E_{fb} - \frac{k_B T}{q}\right). \quad (2)$$

C is the differential capacitance, A is the surface area of the electrode, ε_0 is the vacuum permittivity, ε_r is relative permittivity, q is the electronic charge, N_d is the donor impurity concentration in the semiconductor, E is the applied potential, E_{fb} is the flat band potential, k_B

is the Boltzmann's constant, and T is the temperature (K).

1.6. H/D isotope KIE tests.

H/D isotope KIE tests were carried out in 0.1 M $NaClO_4$ (pH = 11) with H_2O or D_2O as the solvent for WOR. For the AOR process, 0.1 M NH_3 (or ND_3) was added into the H_2O (or D_2O) solvent with 0.1 M $NaClO_4$ as the supporting electrolyte. The pH was tuned by adding $NaOH/HClO_4$ or $NaOD/D_2SO_4$. The steady-state current for each potential was measured using the chronoamperometry method with a duration of 60s. The KIE value was obtained by dividing the current in H_2O by that in D_2O, and the corresponding data was shown in Figure S9.

1.7. TPV tests.

The transient photovoltage (TPV) spectra measurements were carried out using CEL-TPV2000 equipment from Beijing China Education AU-LIGHT Technology Co., Ltd. The tests were conducted in a quartz cell under an open-circuit condition with a 532 nm laser. The TPV instrument was equipped with a preamplifier, which supplied a 20-fold signal gain in our experiments. The electrolytes used were 0.1 M $NaClO_4$ with or without 100 mM NH_3, and the reference electrode was Ag/AgCl.

1.8. TPD tests.

The transient photocurrent decay (TPD) method was used to measure the surface-trapped hole density under high potentials (1.35 V_{RHE}) according to our previous work.[3] The 530 nm LED equipped on the Autolab workstation (PGSTAT302N) was used for illumination with various light intensities. The surface-trapped hole density ($[h^+]$) was obtained via the equation

below:

$$[h^+] = Q_{ss} / (S \times q), \quad (3)$$

where Q_{ss} (C) is the total charge passing through the photoanode during the cathodic transient process as shown in Figure S25, S (nm^2) is the ECSA of the photoanode, and q is the electron charge (1.6×10^{-19} C).

1.9. *Operando* Raman spectra.

For the *operando* PEC Raman (LabRAM Odyssey, HORIBA) experiments, a 532 nm laser was used to probe and excite the surface-active species on various photoanodes. The 50% Neutral Density (ND) filter, 600 grating (500 nm), and 50× visible long-work-distance lens were used during the operation. For all the Raman tests in this work, the Rayleigh and monocrystalline Si signals were calibrated to 0 and 520.75 cm^{-1}, respectively. A customized three-electrode electrochemical cell was used for the *operando* Raman measurements, with Ag/AgCl and Pt wire as the reference electrode and counter electrode, respectively. The electrolyte was 0.1 M $NaClO_4$ with 100 mM NH_3. The exposure time was set to 20 s with 3-times accumulations to obtain steady-state information of surface states, and the applied potential was carried out by the CHI 760e electrochemical workstation.

1.10. Quantitative Raman spectra.

The quantification of NH_3 concentrations ($[NH_3]$) on the electrode surface was achieved by Raman spectra (LabRAM Odyssey, HORIBA) using an external reference method. 532 nm laser, 50% Neutral Density (ND) filter, 1800 grating (500 nm), and 50× visible long-work-

distance lens were used during the operation. For the measurements of Job's plots, a series of NH_3 standard solutions with various [NH_3] were injected into a customized Raman cell, and the laser was focused on the interface of bare Si and solutions. The exposure time was set to 20s with 2-times accumulations. For each measurement, the laser was focused on the point with the maximum peak intensity of Si base (520.75 cm^{-1}) in RTD mode, to eliminate the deviation induced by the changed work distance in different experimental groups. The Raman spectra with various [NH_3] and corresponding Job's plots are shown in Figure S20.

1.11. Products analysis.

The gas products were analyzed by gas chromatography (GC, FULI, 9790Plus) equipped with a 5Å column (60 m × 530 μm) and a TCD detector. The oven temperature was 80 °C. The liquid products were analyzed by ion chromatography (Thermo Fisher, ICS-900) equipped with a Thermo Dionex IonPacTM AS19 anion exchange column (250 mm × 4 mm) and Reagent-FreeTM Controller (Thermo Fisher, RFC30). A gradient eluting procedure was used with 15 mM KOH eluents in the initial 18 min, then the concentration of eluents was increased to 50 mM in 1 min and then kept 50 mM with a duration of 12 min. Both gas and liquid products were quantified with an external reference method, employing the Job's plots as shown in Figure S6. The Faradaic efficiency (FE) was calculated via the equations below:

$$FE_{NO_2^-}(\%) = n(NO_2^-) \times 6 \times F / Q \times 100\%, \quad (4)$$

$$FE_{NO_3^-}(\%) = n(NO_3^-) \times 8 \times F / Q \times 100\%, \quad (5)$$

$$FE_{N_2}(\%) = n(N_2) \times 6 \times F / Q \times 100\%, \quad (6)$$

$$FE_{O_2}(\%) = n(O_2) \times 4 \times F / Q \times 100\%, \quad (7)$$

where n is the mol of corresponding product, F (96500 C/mol) is the Faraday constant, Q (C) is the total passed charge.

2. DFT calculations.

2.1. Quantum chemistry calculations.

The Density Functional Theory (DFT) calculations of molecules for pH-dependent Gibbs free energy were carried out with the ORCA 5.0.4 package.[4-5] The def2-TZVP (with def2/J) basis set and the B3LYP functional in combination with the internal DFT-D3 correction were used for the optimization and frequency calculations. Apart from the gaseous molecules, all other calculations were performed in the framework of the CPCM solvation model with water as the solvent. The thermochemistry corrections were conducted at 1 bar and 298.15 K. The Gibbs free energies of the proton and electron can be described as:

$$G_{H^+} + G_{e^-} = G_{H_2}/2. \quad (8)$$

The effect of pH effect on the ΔG was corrected via the equation below:

$$\Delta G_{pH} = -k_B T \ln[H^+] = pH \times k_B T \ln 10. \quad (9)$$

2.2. First-principles calculations.

The first-principles calculations were carried out using the PBE functional and DZVP basis sets in the CP2K package[6-7], and the dispersion correction was applied in all calculations with the Grimme D3 method[8]. For the $Cu(OH)_2$, a slab model of (002) facet with 20.818 Å × 14.698 Å × 22.032 Å supercell (15 Å vacuum layer) was constructed based on the conventional cell (2.957 Å × 11.282 Å × 5.244 Å). The NiO/Ni/n-Si photoanode was simulated with a

NiOOH model, as it is the real active phase during the AOR according to the experimental results. The $(01\bar{1}2)$ facet of NiOOH was constructed based on the conventional cell of the NiOOH (a = b = 2.978 Å, c = 4.579 Å), and the 4 × 2 × 1 supercell with 15 Å vacuum layer (11.914 Å × 13.796 Å × 24.868 Å) was built for catalytic calculations. The Cu-incorporated NiOOH slab model was constructed by replacing one surface Ni atom of the NiOOH slab model with a Cu atom. The bare surface of the Ni(Cu)OOH slab model was saturated with H_2O molecules, considering the solution environment in practice. The 1 × 2 × 1 *k*-point mesh with the cutoff of 400 Ry and GTH pseudopotential was used for geometry optimization and energy calculations. The energy convergence for the self-consistent field calculation was set to 5×10^{-7} Hartree, and the largest forces on atoms were set less than 4.5×10^{-4} Hartree/Bohr. The transition state (TS) was located with the climbing image nudged elastic band (CI-NEB) method to generate the initial guesses, and saddle points were further converged by the dimer method.

The adsorption energy was calculated via the equation below:

$$E_{ad} = E_{slab+mol} - E_{slab} - E_{mol}. \quad (10)$$

The Ni(Cu)OOH model with 60 H_2O and 1 NH_3 was built for the *ab initio* molecular dynamics (AIMD) simulation. The simulation was carried out in the canonical ensemble (NVT) imposed by a Nose-Hoover thermostat with a target temperature of 330 K. The MD time step is set to 0.5 fs. Only Γ point was used in the AIMD calculation due to the large size of the supercell (11.914 Å × 13.796 Å × 24.868 Å).

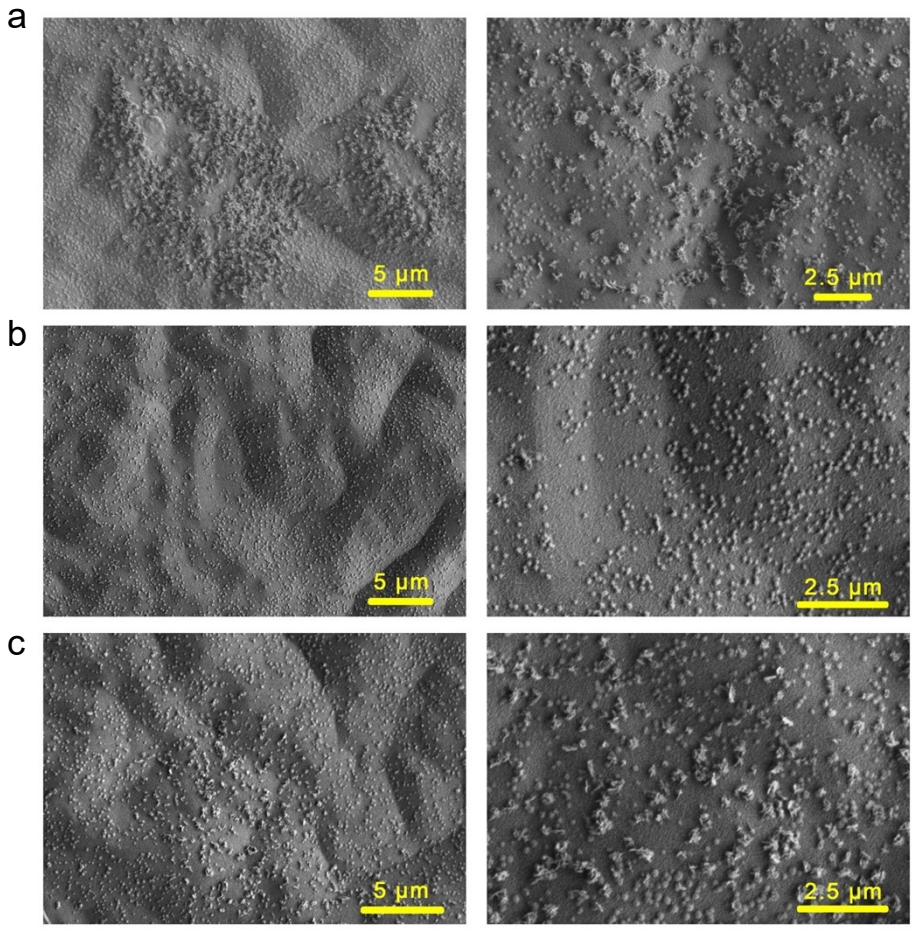

Figure S1. SEM graphs of a) pristine NiO/Ni/n-Si photoanode and that after b) WOR or c) AOR.

As shown in Figure S1a, NiO on the pristine NiO/Ni/n-Si photoanode existed in the form of nanosheets. Such a nanostructure was well maintained after AOR tests (Figure S1c), whereas it was broken by the WOR process (Figure S1b). The NiO nanosheets were absent for the NiO/Ni/n-Si photoanode after WOR, simply retaining the Ni nanoparticles serving as the protection layer. Based on the analysis of inductively coupled plasma-mass spectrometry (ICP-MS), soluble Ni^{2+} of 0.32 ppm was detected in the electrolyte after WOR tests, while only 0.07 ppm of Ni^{2+} was detected in the electrolyte for AOR. These results confirm the significantly enhanced stability of the NiO/Ni/n-Si photoanode caused by the addition of 50 mM NH_3.

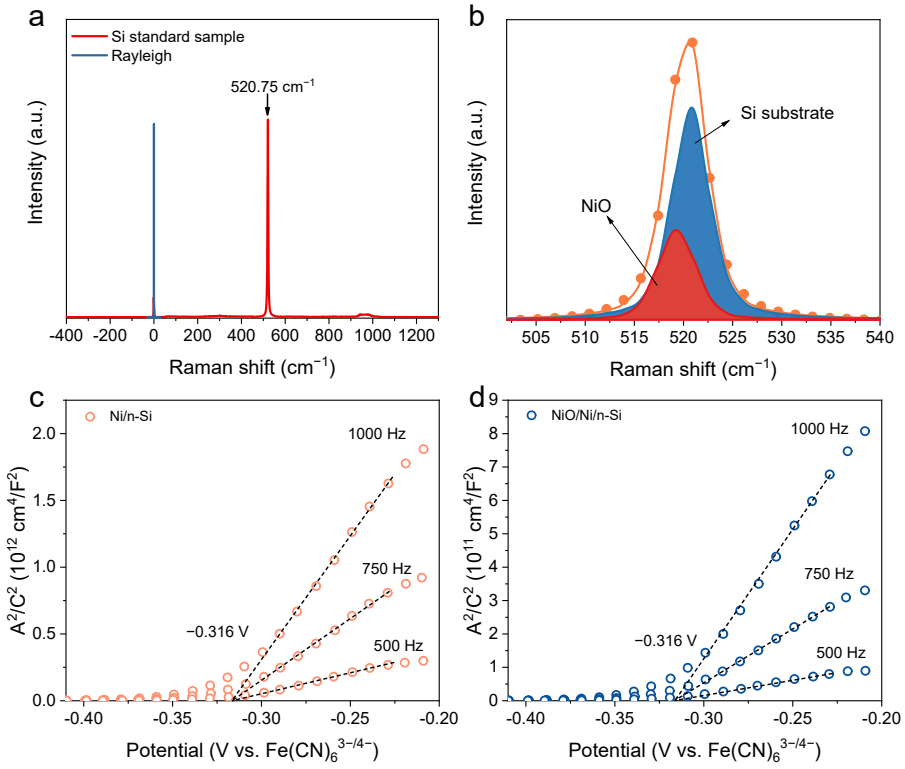

Figure S2. a) Calibration curves of the Raman spectra using monocrystalline silicon standard sample. b) Raman spectrum of NiO/Ni/n-Si photoanode. Mott-Schottky plots of c) Ni/n-Si and d) NiO/Ni/n-Si photoanode.

For all the Raman spectra tests in this work, the Rayleigh and monocrystalline Si signals were calibrated to 0 and 520.75 cm^{-1}, respectively (Figure S2a). The Raman spectrum of dry NiO/Ni/n-Si photoanode was exhibited in Figure S2b, where the signal of NiO at 519 cm^{-1} was identified by Gaussian fitting to differentiate it from the overlapped signals of the Si base.

Mott-Schottky plots of Ni/n-Si and NiO/Ni/n-Si photoanodes are shown in Figure S2c–d. The flat band potentials of both photoanodes were identified as −0.32 V vs. $Fe(CN)_6^{3-/4-}$, indicating that the band structure of the n-Si base was not influenced by the modification of NiO.

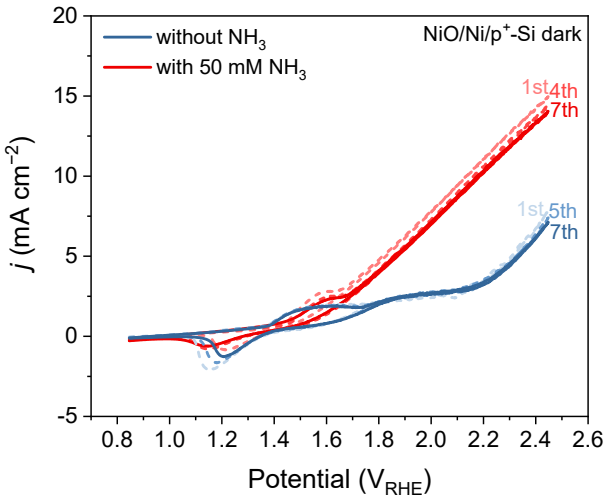

Figure S3. CV profiles of NiO/Ni/p^+-Si with or without 50 mM NH_3 in the dark.

The CV profiles of NiO/Ni/p^+-Si during WOR in the dark did not exhibit significant attenuation at the same level of current density, excluding the influence of bubbles during WOR. Therefore, the detaching of NiO from the NiO/Ni/n-Si photoanode (Figure S1b) should originate from the change in the interface structure during the PEC WOR.

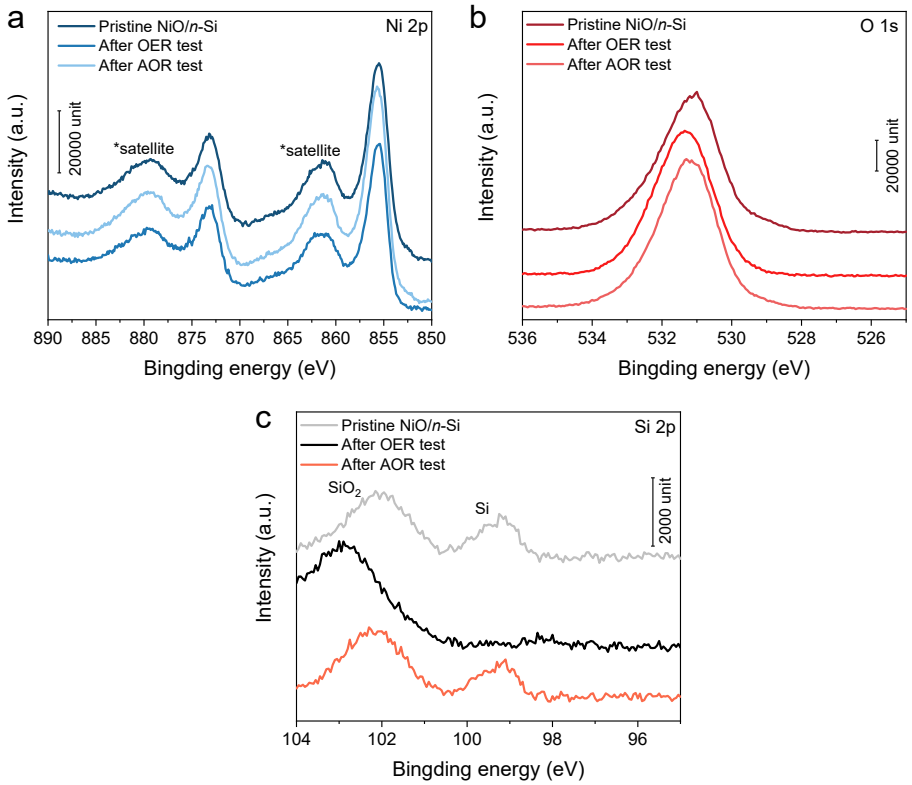

Figure S4. High-resolution XPS of a) Ni 2p b) O 1s, and c) Si 2p of the NiO/Ni/n-Si photoanode before and after WOR or AOR.

The Ni^{2+} was identified by the Ni 2p XPS (Figure S4a). There is no obvious change in the peak position of Ni $2p_{3/2}$ (855.5 eV) for the photoanode before and after AOR or WOR, as the surface of the Ni protection layer was also presented as Ni^{2+}.[9] The O 1s spectra (Figure S4b) displayed a slight shift from 531.01 to 315.25 eV after AOR tests (315.35 eV, after WOR), which derived from the enhancement in adsorbed H_2O.[10] A marked change in the Si 2p spectra[11] was observed for the increased peak intensity of SiO_2 for the photoanode after WOR tests (Figure S4c), indicating serious self-oxidation during WOR. In contrast, the Si 2p XPS showed little changes for the NiO/Ni/n-Si photoanode before and after AOR tests, showing a greatly repressed photocorrosion via the addition of NH_3.

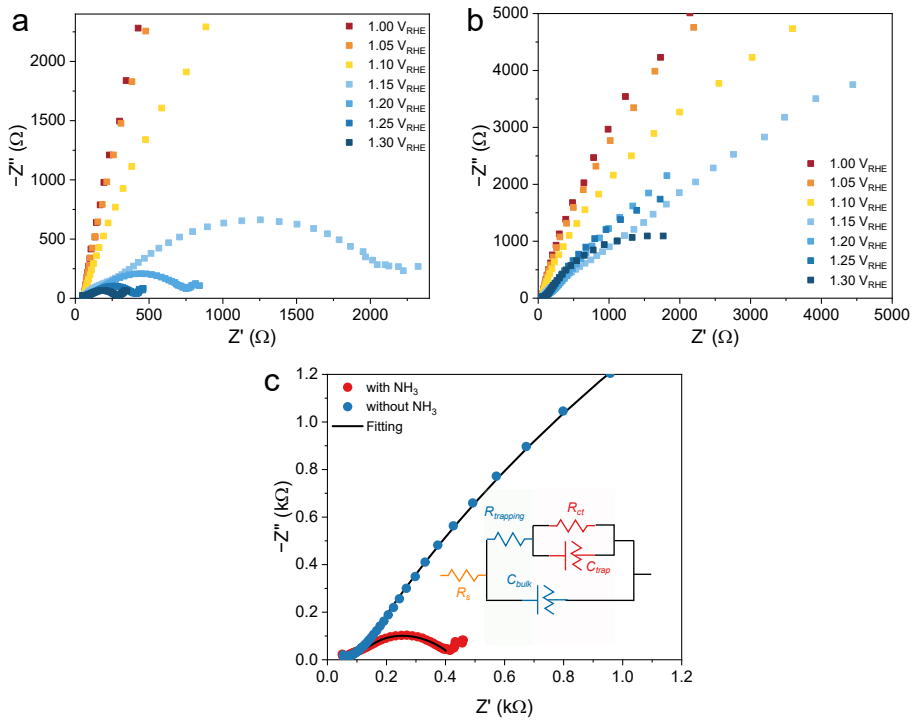

Figure S5. Potential-dependent Nyquist plots of NiO/Ni/n-Si for a) AOR and b) WOR. c) Comparison of fitted Nyquist plots of NiO/Ni/n-Si for AOR and WOR at 1.25 V_{RHE} (inset: equivalent circuit model).

The potential-dependent Nyquist plots of NiO/Ni/n-Si for AOR and WOR are presented in Figure S5a–b, and the fitted results are shown in Table S1 based on the equivalent circuit model in the inset of Figure S5c. For the condition at 1.25 V_{RHE} (Figure S5c), the charge transfer resistance (R_{ct}) for AOR was fitted as 196 Ω, while that for WOR in NH_3-free solution was 9290 Ω. The NH_3-induced faster charge-transfer kinetics restricted the accumulation of holes on the surface of NiO/Ni/n-Si photoanode, thus alleviating the photocorrosion and leading to enhanced stability.

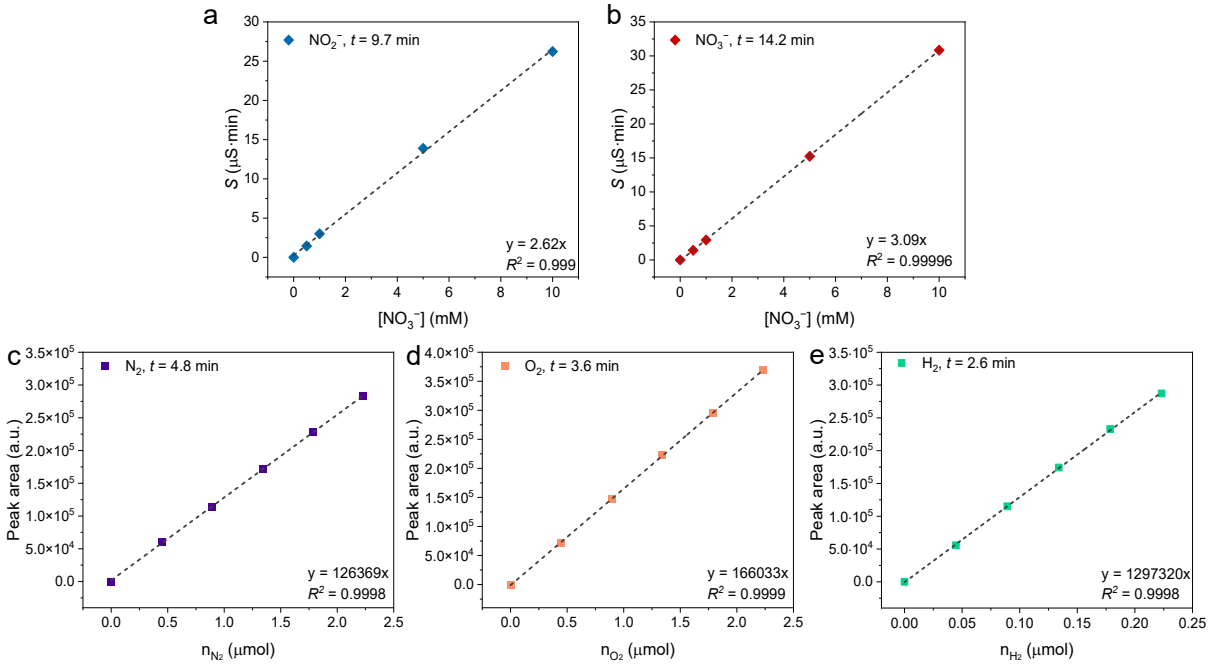

Figure S6. Job's plots for quantification of a) NO_2^-, b) NO_3^-, c) N_2, d) O_2, and e) H_2.

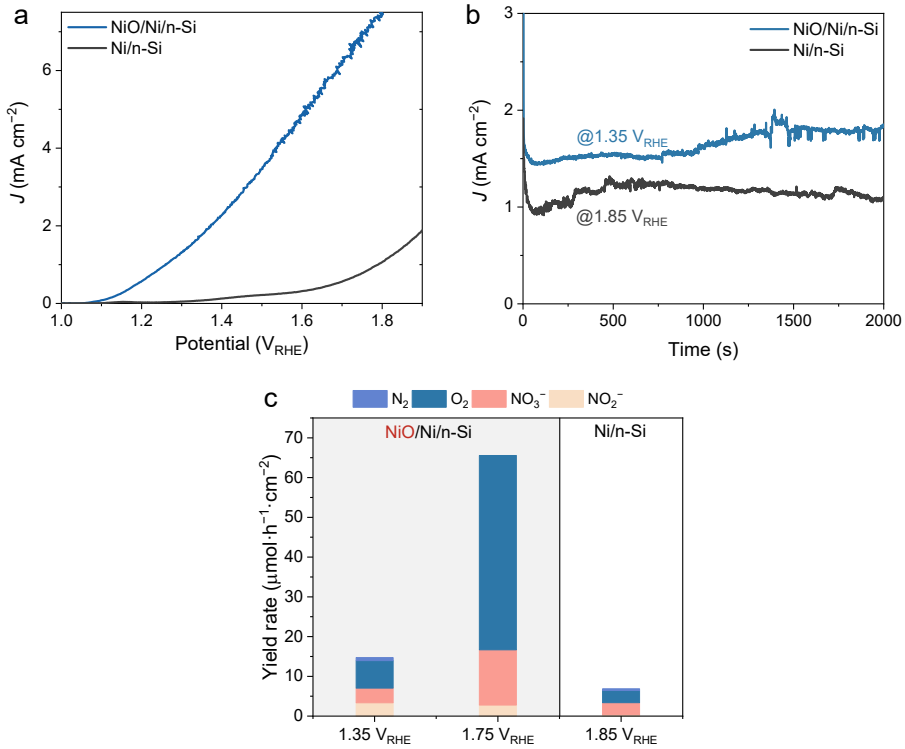

Figure S7. a) *J–V* curves of Ni/n-Si and NiO/Ni/n-Si photoanodes for PEC AOR/WOR in 0.1 M $NaClO_4$ with 0.1 M NH_3. b) *I–T* curves of Ni/n-Si (at 1.85 V_{RHE}) and NiO/Ni/n-Si (at 1.35 V_{RHE}) photoanodes for PEC AOR/WOR. c) Yield rate of oxidation products for Ni/n-Si and NiO/Ni/n-Si photoanodes under various potentials.

The contribution of the Ni protection layer to the AOR/WOR performance of NiO/Ni/n-Si photoanode is negligible when the applied potential <1.6 V_{RHE} according to the *J–V* curves as shown in Figure S7a. Compared with the NiO/Ni/n-Si photoanodes, the Ni/n-Si photoanode displayed a more positive onset potential and lower photocurrent density. To quantify the influence of the Ni protection layer on the PEC performance, we carried out the chronoamperometry electrolysis using Ni/n-Si photoanode. As shown in Figure S7b, the current density of Ni/n-Si at 1.85 V_{RHE} during the chronoamperometry is even lower than that of NiO/Ni/n-Si photoanode at 1.35 V_{RHE}, implying the negligible influence of the Ni protection layer on the AOR performance. In addition, the product analysis was shown in Figure S7c,

where the oxidation products for Ni/n-Si photoanode at 1.85 V_{RHE} were dominated by O_2 and NO_3^-. The total yield rate of oxidation products for Ni/n-Si photoanode at 1.85 V_{RHE} is less than half of that for NiO/Ni/n-Si photoanode at 1.35 V_{RHE}, and it is lower by almost an order of magnitude than that of NiO/Ni/n-Si photoanode at 1.75 V_{RHE}. Notably, the potential window we concern about in this work does not exceed 1.75 V_{RHE}. Hence, the influence originating from the Ni protection layer on the AOR/WOR performance is ignorable.

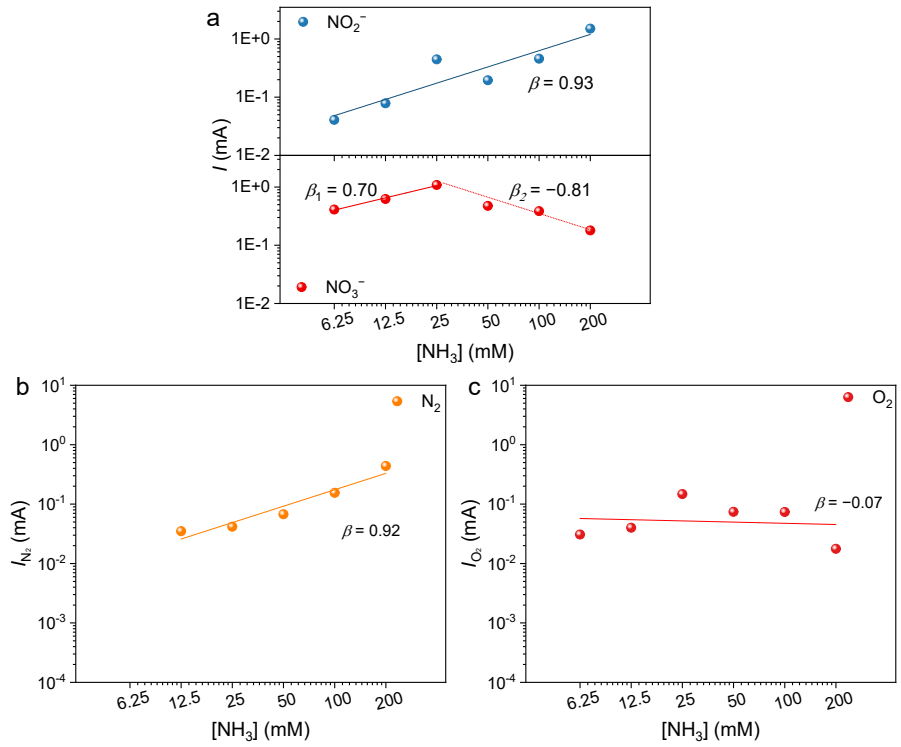

Figure S8. Reaction order of a) NO_2^-, NO_3^-, b) N_2 and c) O_2 for the PEC AOR catalyzed by NiO/Ni/n-Si photoanode at 1.35 V_{RHE} in 0.1 M $NaClO_4$.

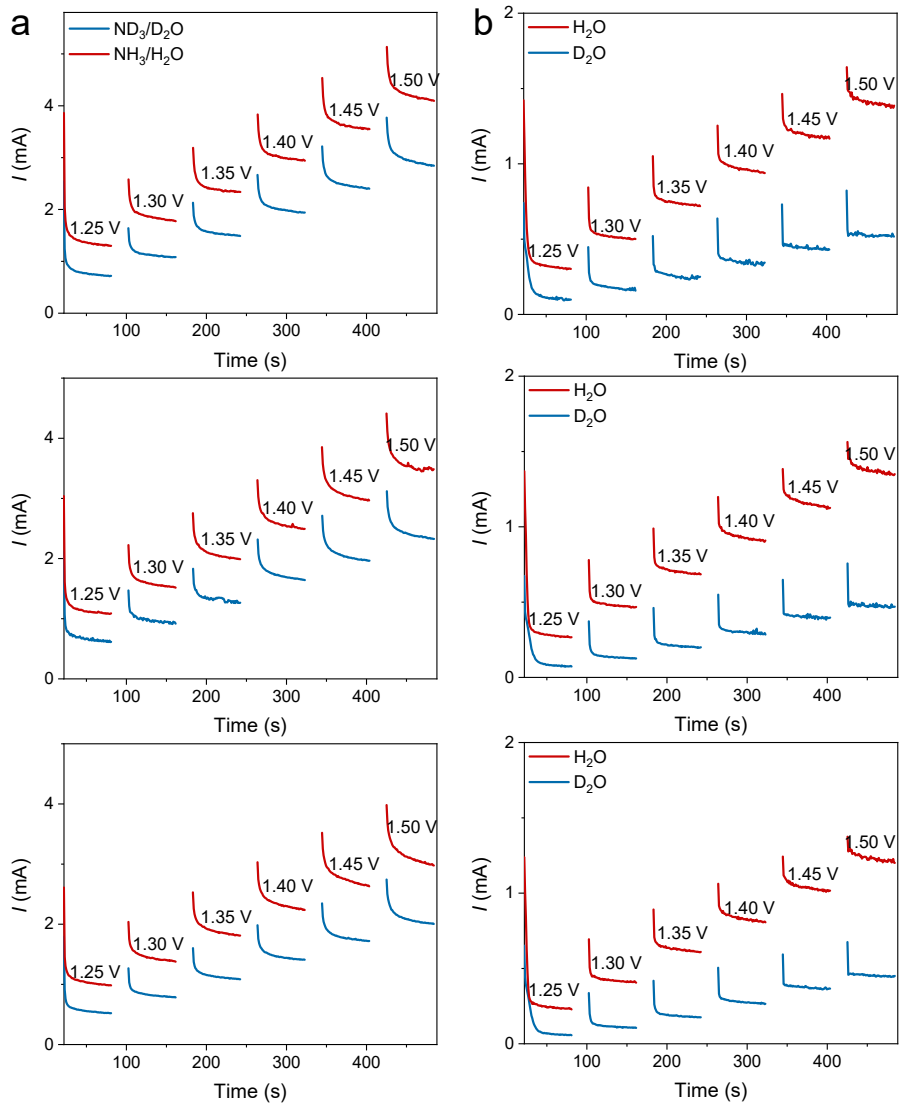

Figure S9. Thrice KIE measurements for a) AOR and b) WOR.

The KIE values for AOR and WOR were calculated according to equations below:

$$\mathrm{KIE} = {}^{I_{NH_3/H_2O}}/_{I_{ND_3/D_2O}}, \tag{11}$$

$$\mathrm{KIE} = {}^{I_{H_2O}}/_{I_{D_2O}}. \tag{12}$$

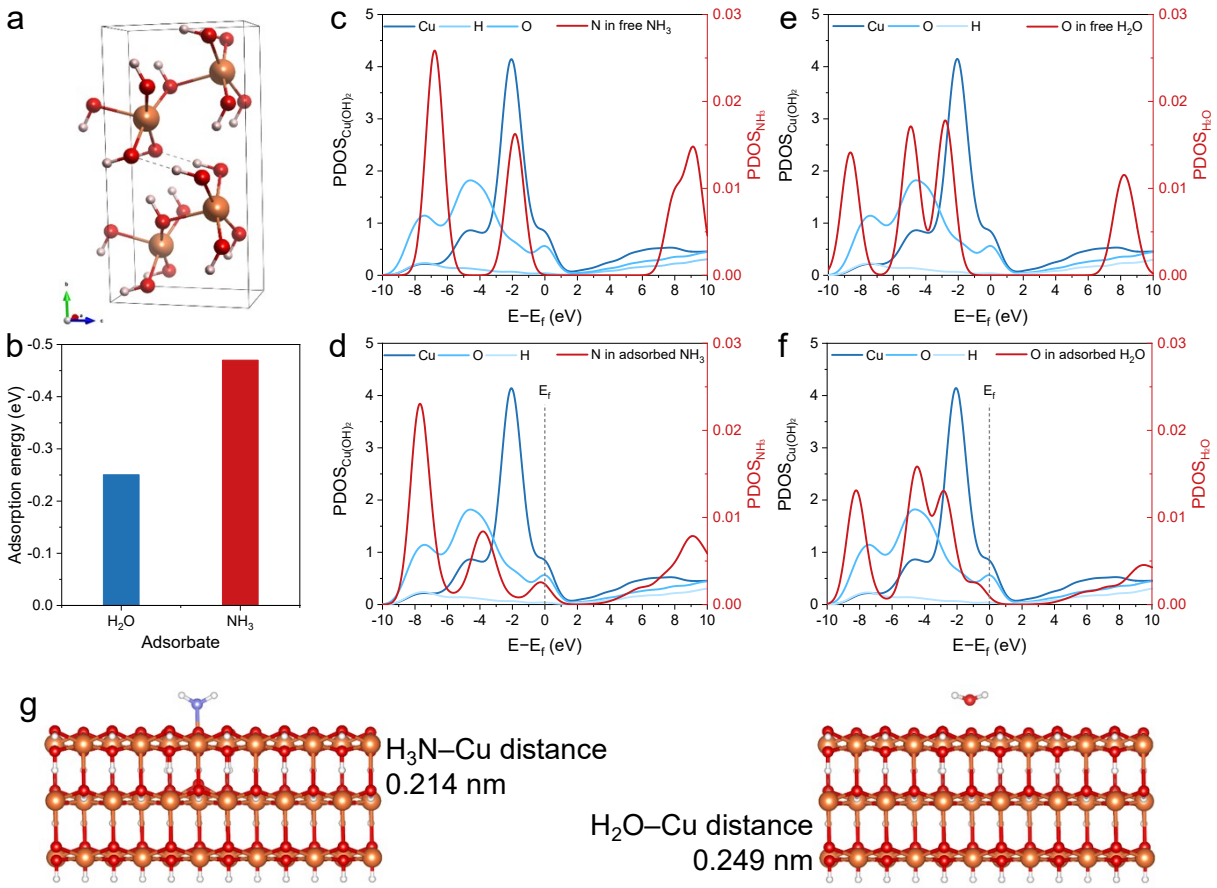

Figure S10. a) Crystal structure of $Cu(OH)_2$. b) Adsorption energy of H_2O and NH_3 on the (001) facet of the $Cu(OH)_2$. Projected density of states (PDOS) for the NH_3–$Cu(OH)_2$ system c) before and d) after the adsorption of NH_3. PDOS for the H_2O–$Cu(OH)_2$ system e) before and f) after the adsorption of H_2O. g) Optimized structure of NH_3–$Cu(OH)_2$ and H_2O–$Cu(OH)_2$ models.

The crystal structure of $Cu(OH)_2$ is shown in Figure S10a, where the Cu atom was found as the 5-coordinated center. The additional adsorption of –OH on the Cu^{II} site would increase its oxidation state (Cu^{III}), whereas it is hard to achieve for the holes from the n-Si photoanode, as the valence band of n-Si was more negative than the redox potential of $Cu^{III/II}$. Hence, the stable form of Cu-base material on the Si photoanode in the basic solution should be Cu^{II}. Such a special coordination structure of $Cu(OH)_2$ inspired us to investigate its adsorption property

for H_2O and NH_3. As shown in Figure S10b, the adsorption energy of NH_3 on the Cu^{II} site was calculated as −0.47 eV, which is almost twice as high as that of H_2O (−0.25 eV), demonstrating stronger interaction between the Cu^{II} site and NH_3 molecule. Orbital analysis based on the Projected density of states (PDOS) calculations unveiled the bonding property between Cu^{II} and NH_3 or H_2O. As shown in Figure S10c, the PDOS of the N atom in a free NH_3 molecule significantly overlapped with that of the Cu^{II} atom, resulting in the strong orbital hybridization of the two atoms after adsorption (Figure S10d). The hybridized N 2p orbital exhibited a similar shape to that of lattice O atoms in the $Cu(OH)_2$, showing the chemical bonding between the NH_3 and $Cu(OH)_2$. By contrast, the O atoms in H_2O displayed a weaker interaction with the Cu^{II} site (Figure S10e–f), which is further demonstrated by the optimized structures. As shown in Figure S10g, the bond length of N–Cu in the optimized structure was 0.214 nm, while the length of O–Cu was much longer (0.249 nm). All these results revealed a stronger interaction between the NH_3 and Cu^{II} sites, which led to the selective adsorption of NH_3 on the Cu^{II}.

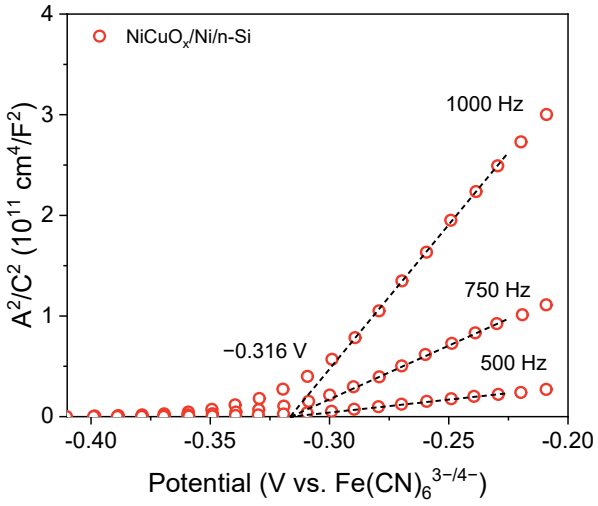

Figure S11. Mott-Schottky plots of $NiCuO_x$/Ni/n-Si photoanode.

Mott-Schottky plots of $NiCuO_x$/Ni/n-Si photoanodes are shown in Figure S11. The flat band potential of $NiCuO_x$/Ni/n-Si photoanode was identified as −0.32 V vs. $Fe(CN)_6^{3-/4-}$, which is the same as that of NiO/Ni/n-Si and Ni/n-Si photoanodes.

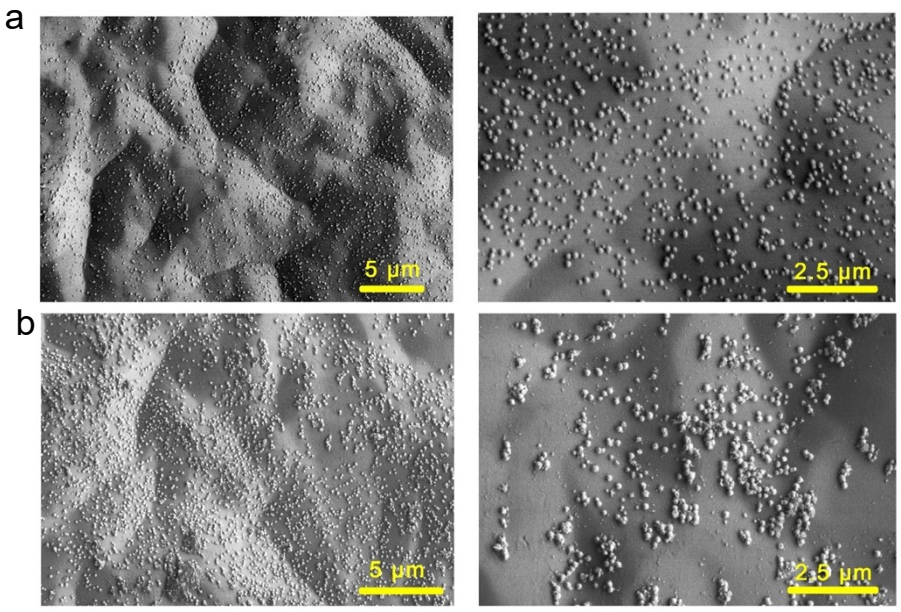

Figure S12. SEM graphs of a) Ni/n-Si and b) CuO_x/Ni/n-Si photoanodes.

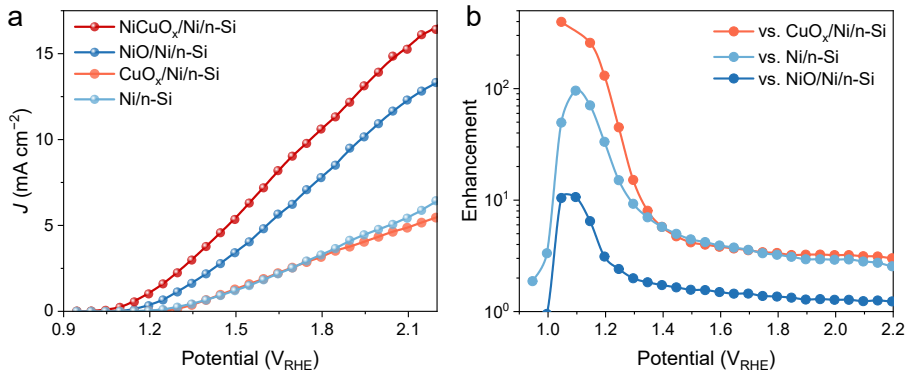

Figure S13. a) Steady-state (record at 60s) AOR *J*–*V* curves of various photoanodes: NiCuO$_x$/Ni/n-Si, NiO/Ni/n-Si, CuO$_x$/Ni/n-Si, and Ni/n-Si tested in 0.1 M $NaClO_4$ with 100 mM NH_3 under AM 1.5 G (100 mW cm^{-2}), and b) enhancement in *J* of NiCuO$_x$/Ni/n-Si versus other Si photoanodes.

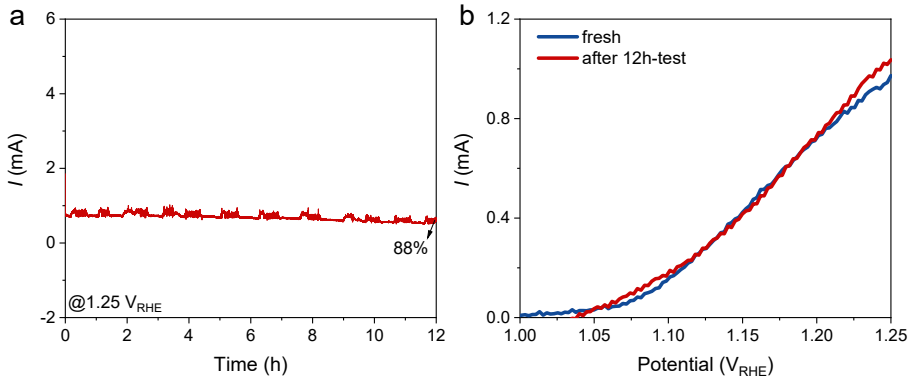

Figure S14. a) *I–T* curve of $NiCuO_x$/Ni/n-Si photoanode during long-time AOR tests and b) LSV curves before and after the tests in 0.1 M $NaClO_4$ with 100 mM NH_3.

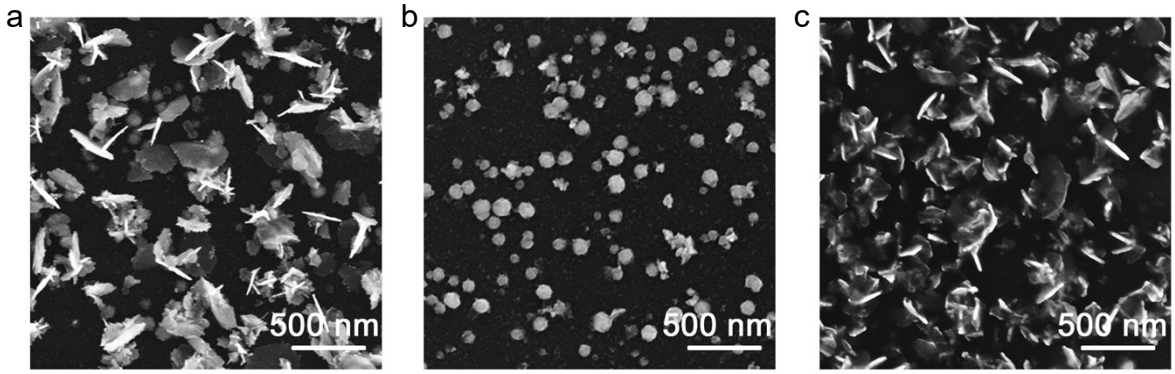

Figure S15. SEM graphs of the a) pristine $NiCuO_x$/Ni/n-Si photoanode and after b) WOR or c) AOR tests.

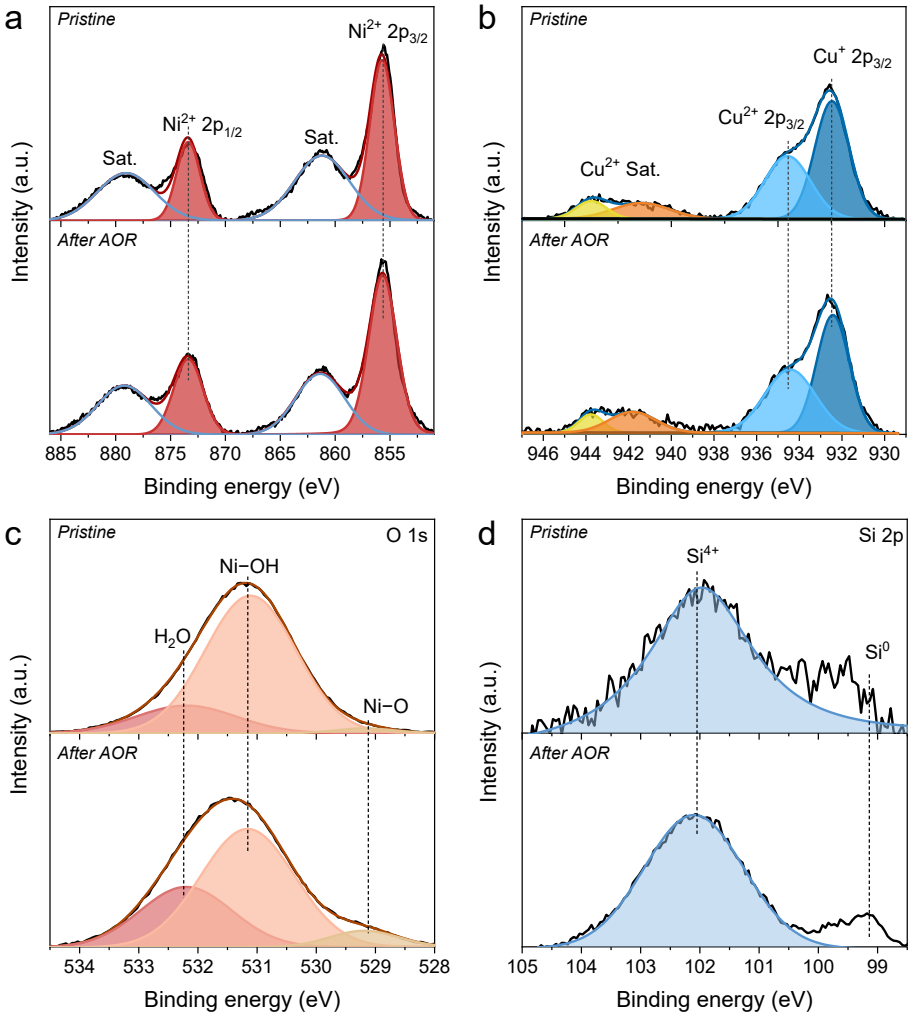

Figure S16. High-resolution XPS of a) Ni 2p b) Cu 2p, c) O 1s, and d) Si 2p of the $NiCuO_x$/Ni/n-Si photoanode before and after AOR.

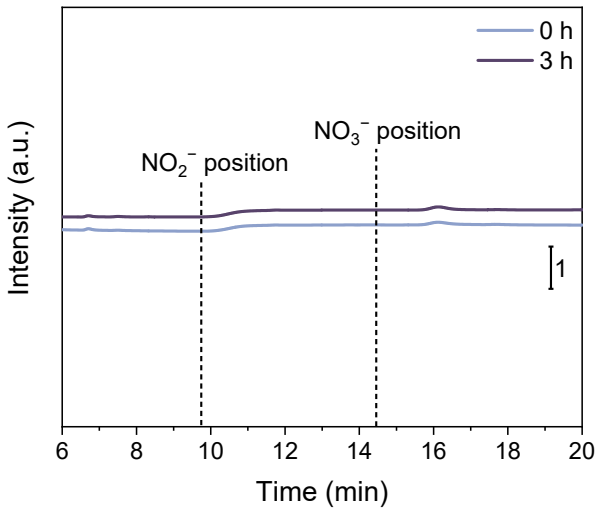

Figure S17. Product detection (ion chromatography data) in the control experiment for photocatalytic AOR using $NiCuO_x$/Ni/n-Si photoanode but without applied potential.

The control experiment without applied bias was carried out to evaluate the influence of the photocatalytic process on the performance of PEC AOR. In theory, it is hard to employ Si-based materials in photocatalytic AOR and WOR processes without sacrificial agents due to their narrow bandgap (~1.1 eV). That is, such a narrow bandgap cannot cover the voltage window for many overall reactions (such as 1.23 V for overall water splitting). Specifically, we conducted the control experiment by illuminating $NiCuO_x$/Ni/n-Si photoanode (AM 1.5 G) for 3h in 0.1 M NH_3 aqueous solution but without applied bias. Then the solution was analyzed with ion chromatography. As shown in Figure S17, the illumination of 3h on the $NiCuO_x$/Ni/n-Si did not produce any detectable AOR products, demonstrating that the measurement would not be affected by the pure photocatalysis process.

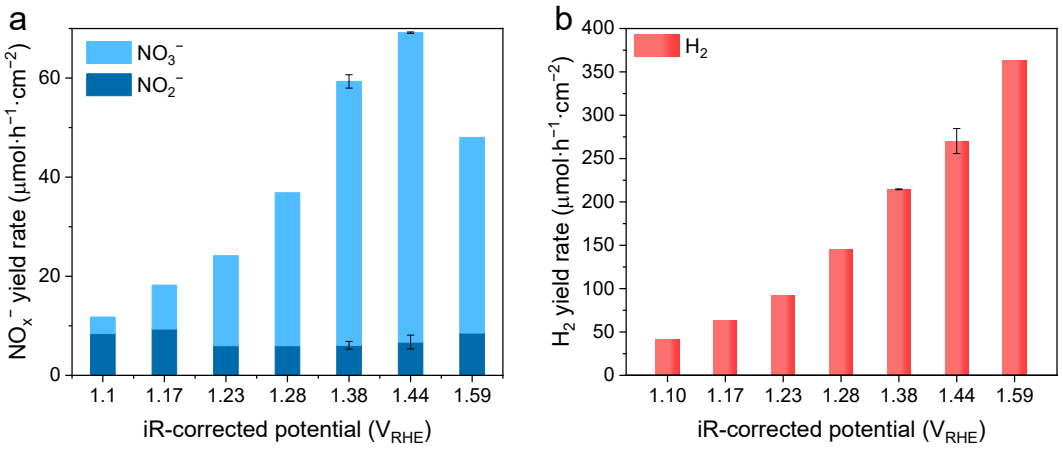

Figure S18. Potential-dependent yield rate (with iR-correction) of a) NO_2^- and NO_3^- on the $NiCuO_x$/Ni/n-Si photoanode and b) H_2 on the Pt cathode in 0.2 M $NaClO_4$ with 150 mM NH_3.

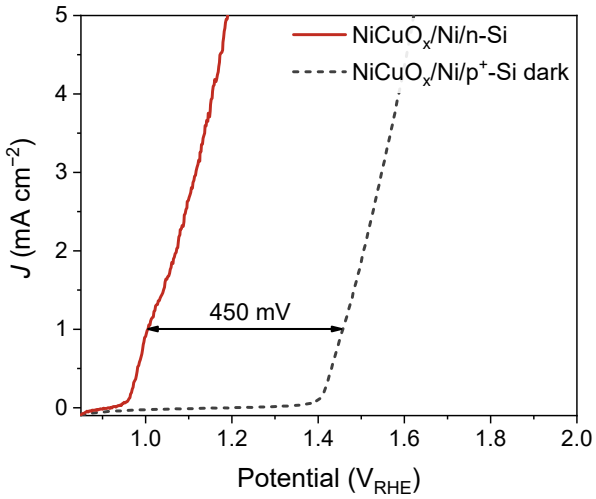

Figure S19. Measurement of the photovoltage of $NiCuO_x$/Ni/n-Si photoanode for AOR with iR-correction.

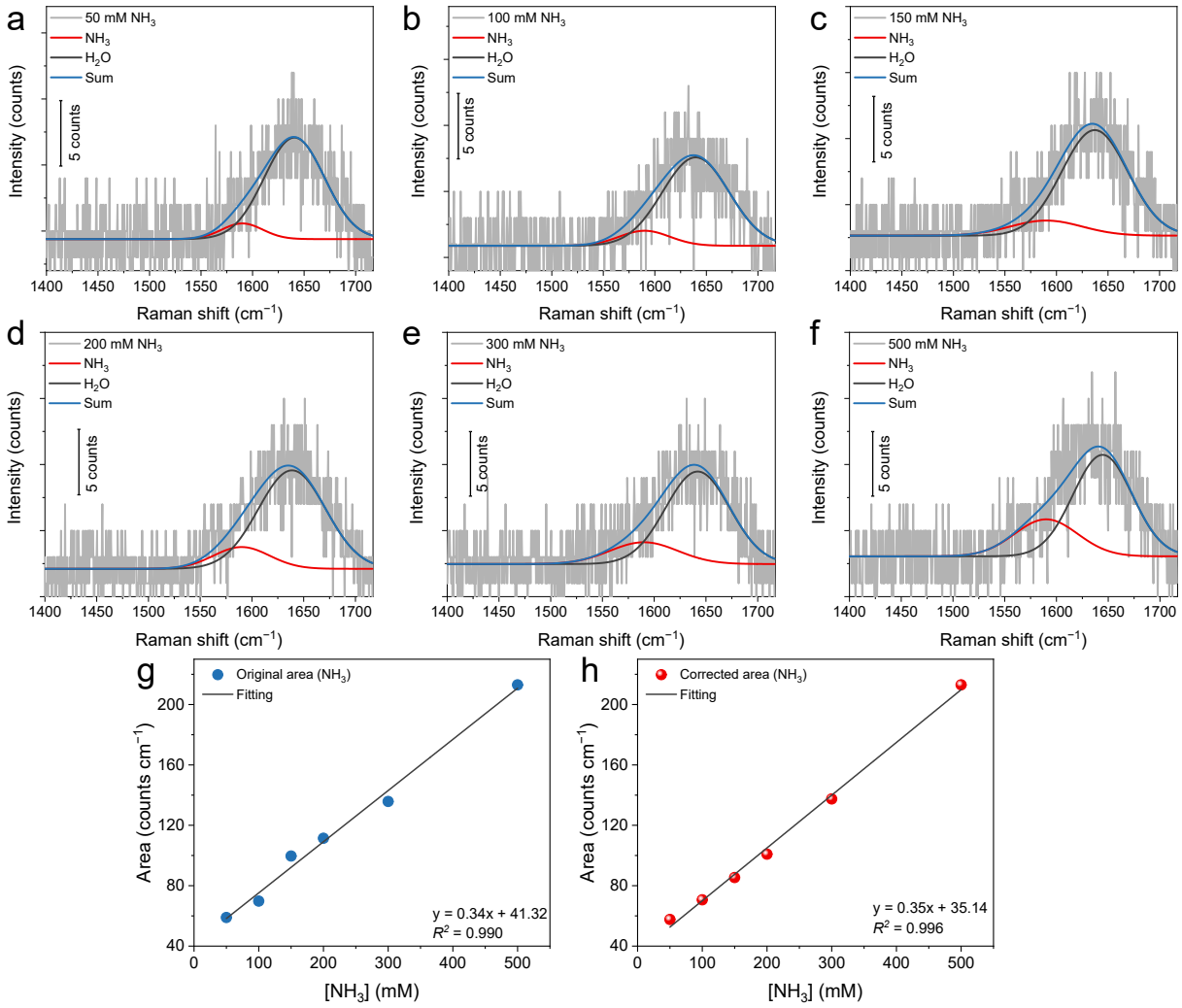

Figure S20. a–f) Raman spectra of NH_3 with various concentrations on the surface of the bare Si. g) Job's plot for quantifying the concentration of NH_3 on photoanodes based on the fitted peak areas. h) Corrected Job's plot by normalizing the peak area of water.

The surface [NH_3] on photoanodes was determined by the Raman spectra (Figure S20a–f) according to the method in *1.10. Quantitative Raman spectra* section. The peak at 1590 cm^{-1} was identified as the NH_3 molecule[12], which was differentiated from the signal of H_2O at ~1638 cm^{-1} and imitated with the Gaussian function. The Job's plot of surface [NH_3] exhibited a good degree of fitting with an R-squared of 0.990 (Figure S20g). In addition, taking into consideration that the mole of H_2O was far more than that of NH_3 in the H_2O/Si interface, the Raman peak area of H_2O should be identical for each test. Accordingly, the fitted peak area of

H_2O in the solution with various [NH_3] was normalized, thereby obtaining the corrected Job's plot of the surface [NH_3]. As shown in Figure S20h, the Job's plot after correction showed an enhanced R-squared of 0.996, demonstrating the feasibility of such a method for the quantification of the surface [NH_3].

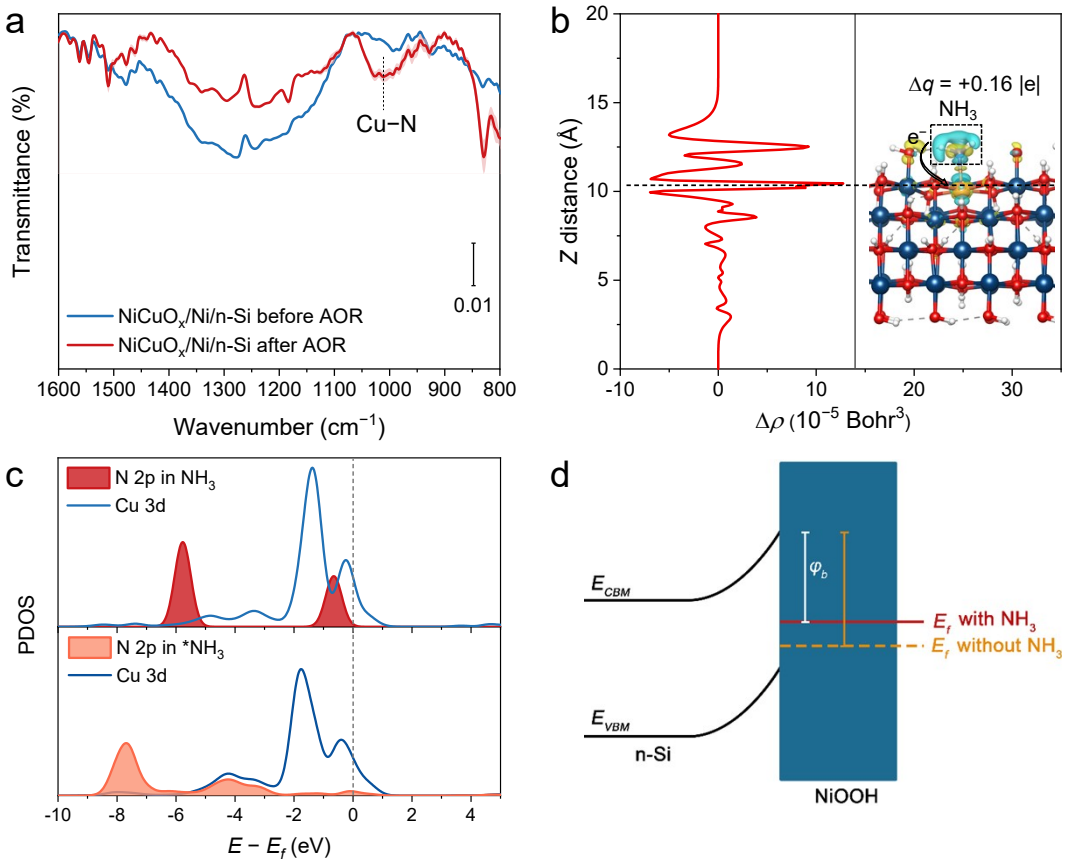

Figure S21. a) Attenuated total reflectance infrared (ATR-IR) spectroscopy of $NiCuO_x$/Ni/n-Si photoanode before and after AOR. b) Charge density difference of $NiCuO_x$/Ni/n-Si photoanode with NH_3 adsorption. c) PDOS of $NiCuO_x$/Ni/n-Si photoanode before and after the NH_3 adsorption. d) Schematics of the Ni/Si interfacial barrier with or without NH_3 adsorption.

The ATR-IR spectroscopy was carried out on the VERTEX 70v FT-IR Spectrometer (Bruker) equipped with a Hyperion3000 microscopy platform. The ATR-IR spectra of the $NiCuO_x$/Ni/n-Si photoanode before and after AOR were measured based on a germanium (Ge) crystal probe. As shown in Figure S21a, the Cu–N bond around 1000 cm^{-1} was identified[13] in the $NiCuO_x$/Ni/n-Si photoanode after AOR, indicating of the adsorption of NH_3 molecules on the Cu sites.

The charge density difference based on the DFT calculations revealed the significant

polarization of the electron density of the NH_3 molecule (Figure S21b), indicating of the strong interaction between the NH_3 and the Cu site in NiOOH. Bader charge analysis showed that the charge of 0.16 |e| was transferred from the NH_3 molecule to the Ni(Cu)OOH fragment, implying that the adsorption of NH_3 resulted in the enhancement of the electron density on the surface of the $NiCuO_x$/Ni/n-Si photoanode. The orbital analysis further demonstrated the strong interaction between NH_3 and the Cu site. As shown in Figure S21c, the PDOS of the N atom in a free NH_3 molecule possessed a similar energy level to the Cu atom, leading to the strong orbital hybridization of the two atoms after the adsorption of the NH_3. The hybridized N 2p orbital in the NH_3 molecule after adsorption almost overlapped exactly with the PDOS of the Cu atom, corresponding to the strong interaction between the NH_3 and Cu site.

Figure S21d presents the schematic of the semiconductor/electrocatalyst interface, where the φ_b is the interfacial barrier height. Generally, the φ_b is dependent on the redox state of the electrocatalyst loaded on the n-Si,[14] which determines the separation and transport dynamics of the photogenerated carriers. For the $NiCuO_x$/Ni/n-Si photoanode in the solution with NH_3, the adsorption of NH_3 increased the surface electron density as discussed above, which lifted the Fermi level (E_f) of the electrocatalyst and thus reduced the φ_b. As a result, a decreased TPV signal for $NiCuO_x$/Ni/n-Si photoanode was observed in the NH_3 solution compared with the NH_3-free case (Figure 4b of the manuscript, Table S3).

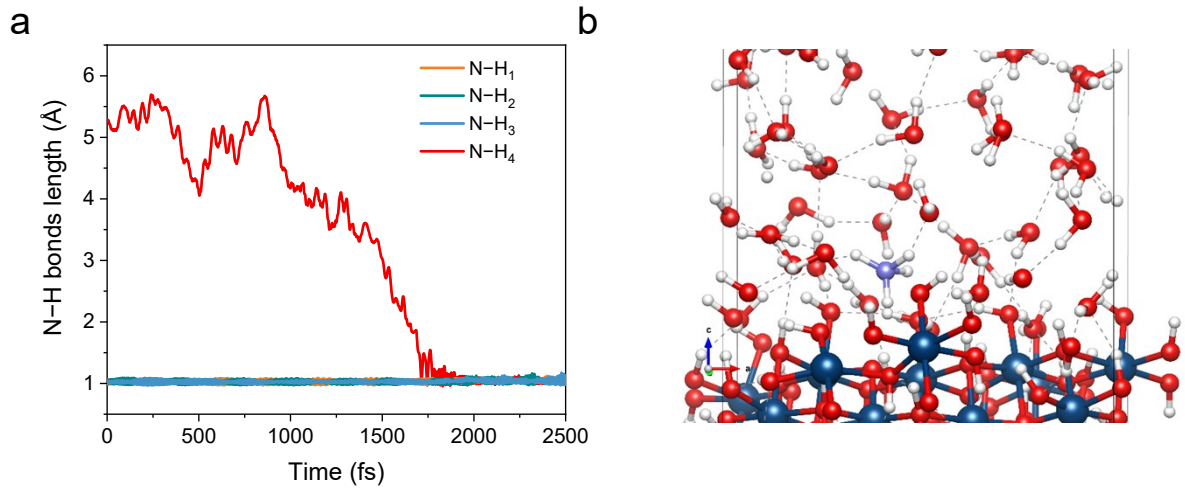

Figure S22. a) Changes in N–H bonds of NH_3 around the surface of NiO/Ni/n-Si photoanode during 2.5 ps AIMD, where H_4 was a proton from the NiOOH as a result of the acid-base equilibrium. b) Structure of simulated NH_3 molecule around the surface of NiO/Ni/n-Si at 2 ps.

The AIMD simulation results based on the NiOOH/electrolyte model without the Cu site are exhibited in Figure S22. Figure S22a elucidates the change in the N–H bond length within the NH_3/NH_4^+ molecule with the simulation time. The initial three N–H bonds in the NH_3 molecule almost maintained their length during the simulation, whereas the distance between the central N atom and an additional H atom decreased from ~5 to ~1 Å after the simulation of ~1.75 ps. By inspecting simulated structure models, the NH_3 molecule was found to capture one of the protons from the NiOOH due to its strong nucleophilicity, thus forming an NH_4^+ ion (Figure S22b). Such an acid-base equilibrium is reversible on a macroscale, so the addition of NH_3 did not have much influence on the TPV signal of the NiO/Ni/n-Si photoanode experimentally. Nevertheless, the oxidation of NH_4^+ is much more difficult than that of NH_3 molecules thermodynamically, which partly accounts for the poor selectivity to AOR products on the NiO/Ni/n-Si photoanode.

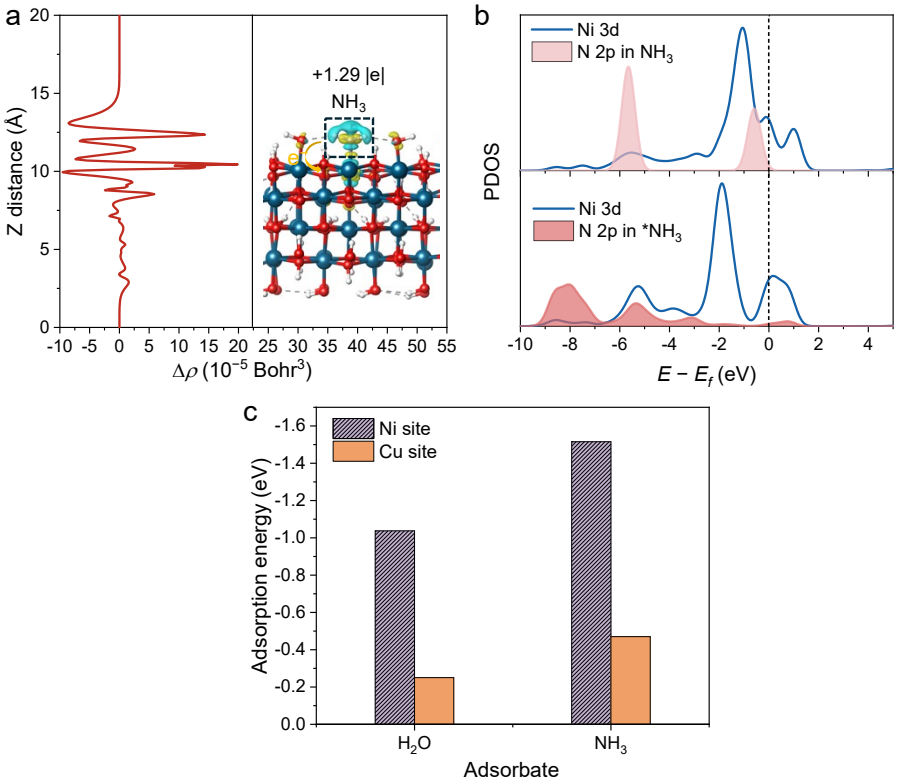

Figure S23. a) Charge density difference of NH_3 molecule adsorbed on the Ni site. b) PDOS of Ni–NH_3 system before and after adsorption. c) Comparison of the adsorption energy of NH_3 and H_2O on Ni or Cu sites.

As shown in Figure S23a, Bader charge analysis shows that +1.29 |e| was transferred from the NH_3 molecule to the catalyst as it adsorbed on the Ni site, indicating of a much stronger interaction between the NH_3 and Ni site compared with that for the Cu site (+0.16 |e|) (Figure S21b). It can be explained by the more electron-deficient *d*-band of the Ni^{III} than that of the Cu^{II} site. The PDOS of N 2p in the NH_3 molecule and Ni 3d site before (top) and after adsorption (bottom) is displayed in Figure S23b. It exhibits a large-extent orbital hybridization between the N 2p molecule and Ni 3d after adsorption, which further demonstrates the strong chemical adsorption of NH_3 on the Ni site.

Nevertheless, the interaction between the NH_3 molecule and Ni site is very weak according to the experimental results of TPV and Raman spectra, which stems from the competitive adsorption between NH_3 and H_2O molecules on the Ni site. As shown in Figure S23c, although the adsorption of NH_3 on the Ni site is easier than that of H_2O due to its stronger nucleophilicity, both of them exhibit larger adsorption energy (< -1.0 eV) on the Ni site compared with that on the Cu site (> -0.5 eV). In light of the much lower concentration of NH_3 in comparison to the H_2O solvent, the adsorption of H_2O on the Ni site is more favorable in actual scenarios. Furthermore, on the basis of Sabatier's principle, once the Ni site is occupied by H_2O, the large adsorption energy of H_2O on the Ni site makes it hard to be replaced by NH_3. Thus, it just presents an insignificant interaction between the NiO/Ni/n-Si photoanode and NH_3, agreeing with the AIMD calculations employing an explicit solvation model (Figure S22). In contrast, the adsorption of H_2O on the Cu site is much weaker, which results in the preferential adsorption of NH_3 on the $NiCuO_x$/Ni/n-Si photoanode.

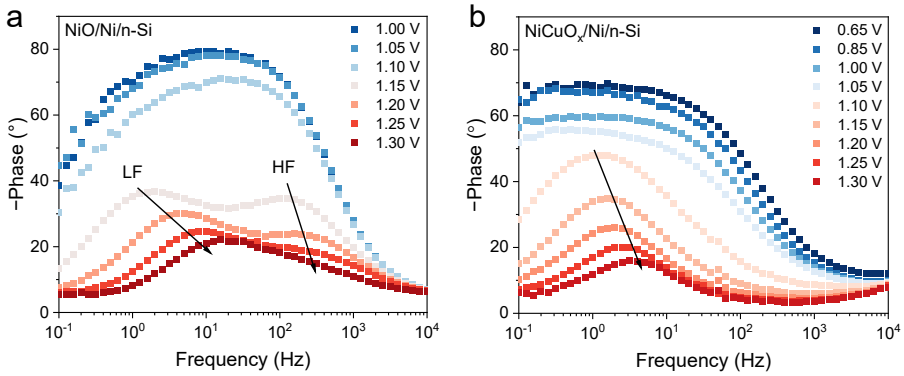

Figure S24. Potential-dependent EIS Bode plots of a) NiO/Ni/n-Si and b) $NiCuO_x$/Ni/n-Si photoanodes during PEC AOR in 0.1 M $NaClO_4$ with 100 mM NH_3.

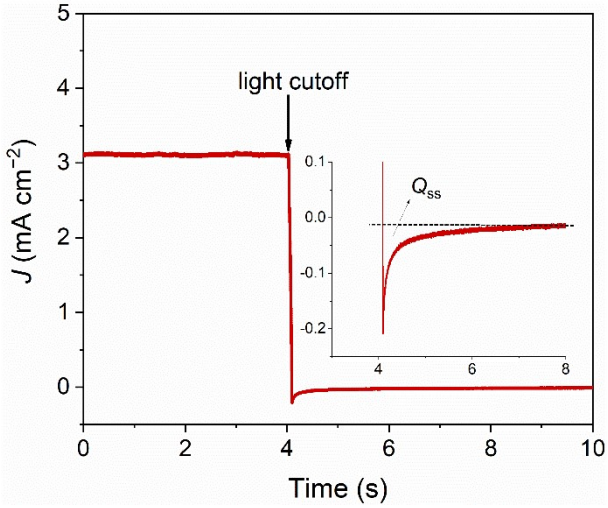

Figure S25. Schematic of the TPD method for the measurement of surface-trapped-hole density.

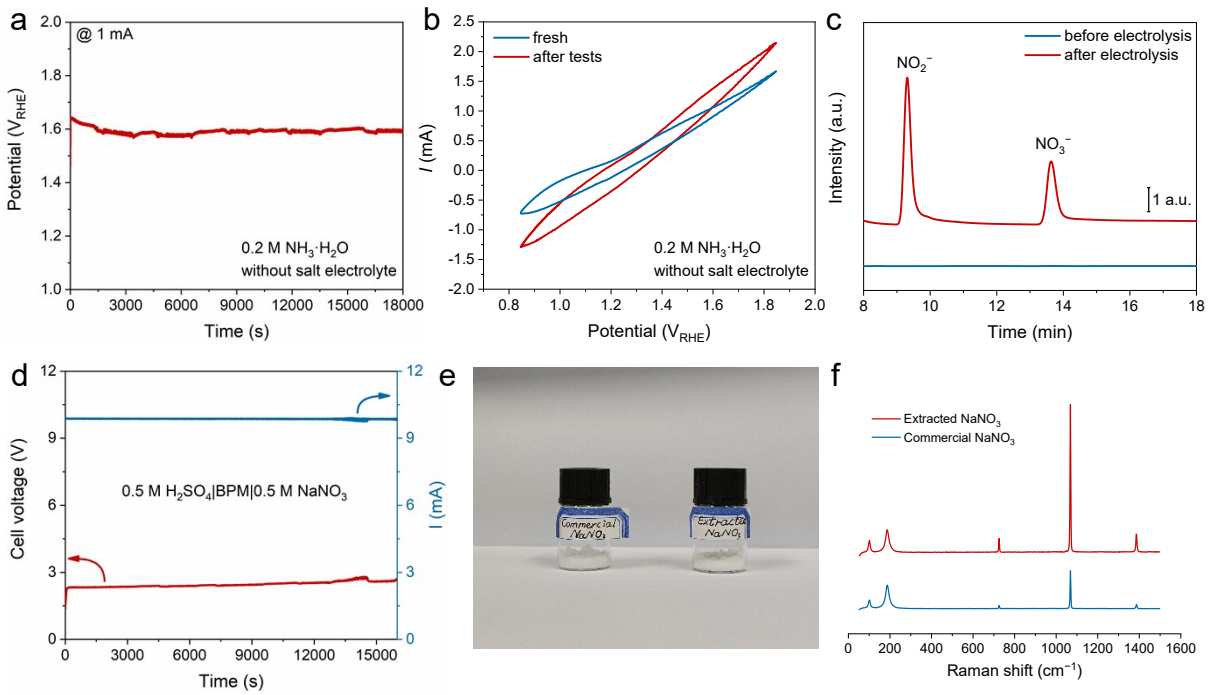

Figure S26. a) PEC electrolysis in 0.2 M NH_3 (pH = 11) without supporting electrolyte. b) CV profiles of $NiCuO_x$/Ni/n-Si photoanode before and after tests in 0.2 M NH_3 without supporting electrolyte, and c) corresponding ion chromatography data. d) Chronopotentiometry curve of the two-electrode PEC electrolysis with 0.2 M NH_3 (pH = 11). e) Optical photograph of the commercial $NaNO_3$ and extracted $NaNO_3$ after PEC electrolysis, and f) corresponding Raman spectra. The two-electrode PEC electrolysis was carried out in an H-cell separated by a bipolar membrane with 0.5 M $NaNO_3$ as the supporting electrolyte of anolyte (0.5 M H_2SO_4 as the catholyte) under 10 mA. Note: The relatively high-concentration electrolytes were adopted here to reduce the Ohmic potential drop in the whole PEC cell. Besides, the NaOH aqueous solution was used to tune the pH of the electrolyte that after the long-term electrolysis to 11, serving as the Na^+ source of the $NaNO_3$ product.

Table S1. Fitted potential-dependent EIS parameters of NiO/Ni/n-Si photoanode with or without 100 mM NH_3 under the illumination of white LED (100 mW·cm^{-2}).

Entry	Potential/V_{RHE}	R_s/Ω	R_{ct}/Ω	C_{trap}/μF	$R_{trapping}$/Ω	C_{bulk}/μF	$[h^+]$/nm^{-2}
With 100 mM NH_3	1.00	57.09	127090.00	0.21	53929.00	9.01	0.00
	1.05	56.71	77019.00	8.98	49926.00	9.18	0.16
	1.10	55.76	54511.00	0.38	7192.20	10.32	0.01
	1.15	53.75	1798.70	116.45	380.02	10.69	2.93
	1.20	52.64	534.03	117.97	181.52	8.47	2.67
	1.25	50.63	196.32	109.19	191.77	7.02	1.66
	1.30	51.89	149.07	53.99	103.66	7.63	0.93
Without NH_3	1.00	58.11	56292.00	0.01	5510.00	4.83	0.00
	1.05	57.96	47140.00	0.00	4093.70	4.93	0.00
	1.10	57.68	38466.00	0.06	2958.30	5.41	0.00
	1.15	55.25	278870.00	28.64	692.27	8.18	0.88
	1.20	52.68	64804.00	221.63	355.25	8.57	7.09
	1.25	56.01	9290.70	326.65	77.84	7.99	10.79
	1.30	56.48	3667.20	269.76	54.54	7.18	9.13

Note: The R_s, $R_{trapping}$, and R_{ct} represent the series resistance, the charge-transport resistance in the surface hole-trapping process and interfacial charge-transfer resistance, respectively. C_{trap} represents the surface state capacitance, and C_{bulk} is the space charge capacitance of the bulk.

Table S2. Comparison of AOR performance for selective NO_x^- synthesis with previously reported photoanodes or electrocatalysts.

Entry	Catalyst	J_{tot}/mA·cm^{-2} @Potential/V_{RHE}	FE(NO_x^-)/ %	J_p(NO_x^-) mA·cm^{-2}	Light	Electrolyte	pH	Reference
1	$NiCuO_x$/Ni/n-Si	2.2 @1.1 V_{RHE}	93.2	2.0	AM 1.5G 100 mW·cm^{-2}	0.2 M $NaClO_4$ +150 mM NH_3	11	this work
2	$NiCuO_x$/Ni/n-Si	12.5 @1.38 V_{RHE}	99.3	12.4	AM 1.5G 100 mW·cm^{-2}	0.2 M $NaClO_4$ +150 mM NH_3	11	this work
3	α-Fe_2O_3	1.3 @1.30 V_{RHE}	45	0.58	AM 1.5G 100 mW·cm^{-2}	0.1 M $NaClO_4$ +100 mM NH_3	10	[15]
4	$BiVO_4$+Cu^{2+}	6.3 @1.23 V_{RHE}	22	1.39	AM 1.5G 100 mW·cm^{-2}	0.3 M $NaClO_4$+200 mM NH_3	10	[16]
5	WO_3	~1.1 @1.23 V_{RHE}	-	0.02	AM 1.5G 100 mW·cm^{-2}	0.1 M Na_2SO_4 +11.3 mM NaCl	4	[17]
6	Au@Pt NPs	0.8 @0.69 V_{RHE}	-	< 0.06	532 nm laser 890 mW·cm^{-2}	1 M NaOH +50 mM NH_3	14	[18]
7	FePi/α-Fe_2O_3	0.95 @1.23 V_{RHE}	-	-	AM 1.5G 100 mW·cm^{-2}	0.1 M NaOH+30 mM NH_3	13	[19]

8	[Ru(bpy-NMe_2)(tpada)(Cl)](PF_6)	~0.015 @1.62 V_{RHE}	~100	~0.015	dark	0.1 M phosphate buffer + 200 mM NH_3	10.86	[20]
9	[Cu(bipyalkH)L](OTf)$_2$	1.2 @2.1 V_{RHE}	93.8	1.12	dark	1 M Na_2SO_4 + 100 mM NH_3	9	[21]
10	CoO_xH_y/ β-NiOOH/ Ni	~10 @1.67 V_{RHE}	77	~7.7	dark	0.1 M K_2HPO_4 + 500 mM NH_3	11.3	[22]
11	$Cu(OH)_2$@ NiOOH	0.8 @1.53 V_{RHE}	88	0.70	dark	0.1 M KOH+10 mM $(NH_4)_2SO_4$	13	[23]
12	Cu rod	2.0 @1.7 V_{RHE}	83	1.66	dark	0.011 M KOH + 100 mM NH_3	-	[24]
		1.0 @1.7 V_{RHE}	81	0.81	dark	0.11 M KOH + 100 mM NH_3	-	
		0.3 @1.7 V_{RHE}	46	0.14	dark	1.1 M KOH + 100 mM NH_3	-	

Table S3. Fitted TPV half-time of photogenerated holes for NiO/Ni/n-Si and $NiCuO_x$/Ni/n-Si photoanode in 0.1 M $NaClO_4$ (pH=11) with or without 100 mM $NH_3 \cdot H_2O$.

Entry			τ_1/μs	τ_2/μs	τ_3/μs
NiO/Ni/n-Si	Without NH_3	rise	0.86	0.86	0.86
		fall	17.64	17.64	51.66
	With NH_3	rise	0.88	0.88	0.88
		fall	16.80	16.80	47.85
$NiCuO_x$/Ni/n-Si	Without NH_3	rise	0.72	0.77	0.77
		fall	0.65	14.06	71.40
	With NH_3	rise	0.55	0.57	0.57
		fall	0.65	10.11	60.43

The half-time of photogenerated holes was fitted with the ExpDecay3 function below:

$$y = y_0 + A_1*\exp(-(x-x_0)/\tau_1) + A_2*\exp(-(x-x_0)/\tau_2) + A_3*\exp(-(x-x_0)/\tau_3)$$

Table S4. TPD measurements for the surface-trapped hole density on the NiO/Ni/n-Si and $NiCuO_x$/Ni/n-Si photoanodes during AOR in 0.1 M $NaClO_4$ (pH=11) with 100 mM $NH_3 \cdot H_2O$ at 1.35 V_{RHE} under various light intensities of 530 nm LED.

Entry	Light intensity/mW·cm^{-2}	Q_{ss}/mC	J/mA·cm^{-2}	[h^+]/nm^{-2}
NiO/Ni/n-Si	100	0.40	2.61	5.09
	80	0.37	2.41	4.66
	60	0.36	2.15	4.56
	40	0.30	1.75	3.82
	20	0.30	1.12	3.73
	10	0.22	0.64	2.73
$NiCuO_x$/Ni/n-Si	100	0.28	3.11	2.89
	80	0.23	2.89	2.36
	60	0.19	2.62	1.92
	40	0.18	2.29	1.83
	20	0.14	1.70	1.40
	10	0.11	1.12	1.11

Table S5. Apparent activation energy measurements during PEC AOR on NiO/Ni/n-Si and $NiCuO_x$/Ni/n-Si photoanodes in 0.1 M $NaClO_4$ (pH=11) with 100 mM $NH_3 \cdot H_2O$ at 1.35 V_{RHE} under the illumination of AM 1.5G (100 mW cm^{-2}).

Entry	*T*/K	*J*/mA·cm^{-2}
NiO/Ni/n-Si	303.15	1.21
	313.15	1.52
	323.15	1.98
	333.15	2.77
$NiCuO_x$/Ni/n-Si	303.15	3.81
	313.15	3.81
	323.15	3.87
	333.15	3.91

Reference

1. Zhang, Y.; Zhang, H.; Liu, A.; Chen, C.; Song, W.; Zhao, J., Rate-Limiting O–O Bond Formation Pathways for Water Oxidation on Hematite Photoanode. *J. Am. Chem. Soc.* **2018,** *140*, 3264–3269.
2. Schalenbach, M.; Raijmakers, L.; Selmert, V.; Kretzschmar, A.; Durmus, Y. E.; Tempel, H.; Eichel, R.-A., How Microstructures, Oxide Layers, and Charge Transfer Reactions influence Double Layer Capacitances. *Phys. Chem. Chem. Phys.* **2024**, DOI: 10.1039/D3CP04743A.
3. Liu, S.; Wu, L.; Tang, D.; Xue, J.; Dang, K.; He, H.; Bai, S.; Ji, H.; Chen, C.; Zhang, Y.; Zhao, J., Transition from Sequential to Concerted Proton-Coupled Electron Transfer of Water Oxidation on Semiconductor Photoanodes. *J. Am. Chem. Soc.* **2023,** *145*, 23849−23858.
4. Neese, F., Software update: the ORCA program system, version 4.0. *WIREs Comput. Mol. Sci.* **2017,** *8*, e1327.
5. Neese, F., Software update: The ORCA program system—Version 5.0. *WIREs Comput. Mol. Sci.* **2022,** *12*, e1606.
6. VandeVondele, J.; Krack, M.; Mohamed, F.; Parrinello, M.; Chassaing, T.; Hutter, J., Quickstep: Fast and accurate density functional calculations using a mixed Gaussian and plane waves approach. *Comput. Phys. Commun.* **2005,** *167*, 103-128.
7. Hutter, J.; Iannuzzi, M.; Schiffmann, F.; VandeVondele, J., cp2k: atomistic simulations of condensed matter systems. *WIREs Comput. Mol. Sci.* **2013,** *4*, 15-25.
8. Grimme, S.; Ehrlich, S.; Goerigk, L., Effect of the damping function in dispersion corrected density functional theory. *J. Comput. Chem.* **2011,** *32*, 1456-65.
9. Fan, K.; Chen, H.; Ji, Y.; Huang, H.; Claesson, P. M.; Daniel, Q.; Philippe, B.; Rensmo, H.; Li, F.; Luo, Y.; Sun, L., Nickel-vanadium monolayer double hydroxide for efficient electrochemical water oxidation. *Nat. Commun.* **2016,** *7*, 11981.
10. Zhang, N.; Hu, Y.; An, L.; Li, Q.; Yin, J.; Li, J.; Yang, R.; Lu, M.; Zhang, S.; Xi, P.; Yan, C. H., Surface Activation and Ni-S Stabilization in NiO/NiS(2) for Efficient Oxygen Evolution Reaction. *Angew. Chem., Int. Ed.* **2022,** *61*, e202207217.
11. Laskowski, F. A. L.; Nellist, M. R.; Venkatkarthick, R.; Boettcher, S. W., Junction behavior of n-Si photoanodes protected by thin Ni elucidated from dual working electrode photoelectrochemistry. *Energy Environ. Sci.* **2017,** *10*, 570−579.
12. Butcher, D. P.; Gewirth, A. A., Nitrate reduction pathways on Cu single crystal surfaces: Effect of oxide and Cl^-. *Nano Energy* **2016,** *29*, 457–465.
13. Xie, X.; Zhang, X.; Xie, M.; Xiong, L.; Sun, H.; Lu, Y.; Mu, Q.; Rummeli, M. H.; Xu, J.; Li, S.; Zhong, J.; Deng, Z.; Ma, B.; Cheng, T.; Goddard, W. A., 3rd; Peng, Y., Au-activated N motifs in non-coherent cupric porphyrin metal organic frameworks for promoting and stabilizing ethylene production. *Nat. Commun.* **2022,** *13*, 63.
14. Laskowski, F. A. L.; Oener, S. Z.; Nellist, M. R.; Gordon, A. M.; Bain, D. C.; Fehrs, J. L.; Boettcher, S. W., Nanoscale semiconductor/catalyst interfaces in photoelectrochemistry. *Nat. Mater.* **2020,** *19*, 69–76.
15. Wu, L.; Tang, D.; Xue, J.; Liu, S.; Wang, J.; Ji, H.; Chen, C.; Zhang, Y.; Zhao, J., Competitive Non-Radical Nucleophilic Attack Pathways for NH_3 Oxidation and H_2O Oxidation on Hematite Photoanodes. *Angew. Chem., Int. Ed.* **2022,** *61*, e202214580.

16. Wu, L.; Li, Q.; Dang, K.; Tang, D.; Chen, C.; Zhang, Y.; Zhao, J., Highly Selective Ammonia Oxidation on $BiVO_4$ Photoanodes Co-catalyzed by Trace Amounts of Copper Ions. *Angew. Chem., Int. Ed.* **2024,** *63*, e202316218.
17. Ji, Y.; Bai, J.; Li, J.; Luo, T.; Qiao, L.; Zeng, Q.; Zhou, B., Highly selective transformation of ammonia nitrogen to N_2 based on a novel solar-driven photoelectrocatalytic-chlorine radical reactions system. *Water. Res.* **2017,** *125*, 512–519.
18. Wang, J.; Heo, J.; Chen, C.; Wilson, A. J.; Jain, P. K., Ammonia Oxidation Enhanced by Photopotential Generated by Plasmonic Excitation of a Bimetallic Electrocatalyst. *Angew. Chem., Int. Ed.* **2020,** *59*, 18430–18434.
19. Xia, C.; Li, Y.; Kim, H.; Kim, K.; Choe, W. S.; Kim, J. K.; Park, J. H., A Highly Activated Iron Phosphate Over-layer for Enhancing Photoelectrochemical Ammonia Decomposition. *J. Hazard. Mater.* **2021,** *408*, 124900.
20. Roithmeyer, H.; Severy, L.; Moehl, T.; Spingler, B.; Blacque, O.; Fox, T.; Iannuzzi, M.; Tilley, S. D., Electrocatalytic Ammonia Oxidation with a Tailored Molecular Catalyst Heterogenized via Surface Host-Guest Complexation. *J. Am. Chem. Soc.* **2024,** *146*, 430−436.
21. Liu, H. Y.; Lant, H. M. C.; Troiano, J. L.; Hu, G.; Mercado, B. Q.; Crabtree, R. H.; Brudvig, G. W., Electrocatalytic, Homogeneous Ammonia Oxidation in Water to Nitrate and Nitrite with a Copper Complex. *J. Am. Chem. Soc.* **2022,** *144*, 8449−8453.
22. Cohen, S.; Johnston, S.; Nguyen, C. K.; Nguyen, T. D.; Hoogeveen, D. A.; Van Zeil, D.; Giddey, S.; Simonov, A. N.; MacFarlane, D. R., A CoOxHy/β-NiOOH electrocatalyst for robust ammonia oxidation to nitrite and nitrate. *Green Chem.* **2023,** *25*, 7157−7165.
23. Jiang, X.; Ying, D.; Liu, X.; Liu, M.; Zhou, S.; Guo, C.; Zhao, G.; Wang, Y.; Jia, J., Identification of the role of Cu site in Ni-Cu hydroxide for robust and high selective electrochemical ammonia oxidation to nitrite. *Electrochim. Acta* **2020,** *345*, 136157.
24. Johnston, S.; Kemp, L.; Turay, B.; Simonov, A. N.; Suryanto, B. H. R.; MacFarlane, D. R., Copper-Catalyzed Electrosynthesis of Nitrite and Nitrate from Ammonia: Tuning the Selectivity via an Interplay Between Homogeneous and Heterogeneous Catalysis. *ChemSusChem* **2021,** *14*, 4793−4801.